3D ELASTIC FULL WAVEFORM INVERSION OF SMALL-SCALE HETEROGENEITIES IN TRANSMISSION GEOMETRY

S. Dunkl, A. Kurzmann and T. Bohlen

email: *simone.dunkl@kit.edu*

keywords: *3D, elastic, full waveform inversion, synthetic, random medium, acquisition geometry*

ABSTRACT

3D elastic full waveform inversion aims to reconstruct elastic material properties of 3D structures in the subsurface with high resolution. Here we present an implementation of 3D elastic full waveform inversion based on the adjoint gradient method. The code is optimized regarding runtime and storage costs by using a time-frequency approach. Wavefields are simulated in time domain using Finite-Differences, whereas gradients are calculated in frequency domain. We show synthetic inversion results of P- and S-wave velocities, comparing two transmission geometries: (1) a 3D acquisition geometry with planes of sources and receivers and (2) a 2D geometry with two lines of sources and receivers, resembling two boreholes. Using the 3D geometry, the 3D inversion is capable to resolve differently sized 3D structures in good resolution. The 3D random medium data recorded with 2D acquisition geometry was inverted with the 3D inversion and a 2D full waveform inversion for comparison. The 2D inversion is only capable to resolve the main structures and suffers from artefacts that are caused by the 3D scattering. The 3D inversion offers a comparable resolution within source-receiver plane. Furthermore, when inverting multicomponent data, it is capable to reconstruct main 3D structures up to about 1 to 2 wavelengths adjacent to the source-receiver plane.

INTRODUCTION

In the 1980's Tarantola (1984) and Mora (1987) developed a new inversion strategy known as adjoint full waveform inversion (FWI). By iteratively minimizing the misfit between observed and modeled seismograms this technique uses the full information content given by the waveforms. However, the method is computationally highly demanding and only in recent years, with ongoing increase of computational power available to academia, its application to 3D complex media comes into reach. As wave propagation is influenced by various factors like elastic moduli, density, attenuation and anisotropy, it is necessary to include these parameters in modeling and inversion (Virieux and Operto, 2009). This is a great computational challenge, but offers the opportunity to invert for multiparameters of 3D complex structures. Today, due to computational reasons, many 3D applications still use acoustic modeling, hereby neglecting elastic effects. This is especially the case for marine 3D real data applications (e.g. Plessix, 2009; Sirgue et al., 2010; Vigh et al., 2011; Etienne et al., 2012). The acoustic approximation generally performs well for marine streamer data, but is limited for land seismic and ocean bottom seismic data due to the importance of shear-waves.
Until today most elastic FWI applications are mainly performed in 2D (e.g. Sheen et al., 2006; Groos et al., 2012; Köhn et al., 2012). The 2D approximation is unable to explain 3D scattering arising from 3D heterogeneous subsurface structures and of course only offers insights into one or few 2D slices of the 3D subsurface. 3D elastic FWI is still a computational challenge and applications, as performed by Epanomeritakis et al. (2008), Pyun et al. (2008), Fichtner et al. (2009) and Tape et al. (2010), are rare.
In this work, we describe our first implementation of 3D elastic FWI and show its performance for a 3D

heterogeneous random medium model. Hereby we invert for the compressional and shear wave velocities using a transmission geometry. We study the resolution of 2D and 3D acquisition geometries and compare results of 2D and 3D FWI.

METHOD AND IMPLEMENTATION

Full waveform inversion (FWI) aims to minimize the misfit between modeled data **u** and observed data $\mathbf{u}_{obs}$. This optimisation problem can be solved by the conjugate gradient approach. In each iteration k the model $\mathbf{m}_k$ is updated by

$$\mathbf{m}_{k+1} = \mathbf{m}_k - \alpha_k \mathbf{P}\mathbf{p}_k \tag{1}$$

with preconditioning operator **P** and steplength α_k. The search direction

$$\mathbf{p}_k = \delta\mathbf{m}_k + \beta_k \mathbf{p}_{k-1}. \tag{2}$$

is along the conjugate direction of the gradient of the misfit function $\delta\mathbf{m}_k = \frac{\partial M}{\partial \mathbf{m}}$. The factor β_k is calculated as given in Mora (1987). M denotes the misfit function.
The gradient is calculated using the adjoint method (e.g. Tarantola, 1984; Mora, 1987). The following equations use the Einstein notation. We use the L_2 norm based misfit function given by

$$M = \frac{1}{2} \sum_{sources} \int dt \sum_{receivers} \delta u_i(\mathbf{x}_s, \mathbf{x}_r, t) \delta u_i(\mathbf{x}_s, \mathbf{x}_r, t) \tag{3}$$

with the i-th component of the residual $\delta u_i = u_i - u_{i,obs}$ at source position $\mathbf{x}_s$ and receiver position $\mathbf{x}_r$.
Expressions for the gradients in time or frequency domain are derived in various papers like Mora (1987), Tarantola (1988) and Pratt et al. (1998). We use a time-frequency approach and calculate wavefields in time domain, but do the gradient calculation in frequency domain as described by Sirgue et al. (2008). For a model parametrisation with density ρ and Lamé parameters λ and μ the gradients for one frequency in the frequency domain are given by

$$\delta\rho(\mathbf{x}, \omega) = \sum_s Re[\omega^2 \tilde{u}_i(\mathbf{x}, \mathbf{x}_s, \omega) \tilde{\Psi}_i(\mathbf{x}, \mathbf{x}_s, \omega)], \tag{4}$$

$$\delta\lambda(\mathbf{x}, \omega) = -\sum_s Re\left[\frac{\partial \tilde{u}_i}{\partial x_i}(\mathbf{x}, \mathbf{x}_s, \omega) \frac{\partial \tilde{\Psi}_j}{\partial x_j}(\mathbf{x}, \mathbf{x}_s, \omega)\right] \tag{5}$$

and

$$\delta\mu(\mathbf{x}, \omega) = -\frac{1}{2} \sum_s Re\left[\left(\frac{\partial \tilde{u}_i}{\partial x_j}(\mathbf{x}, \mathbf{x}_s, \omega) + \frac{\partial \tilde{u}_j}{\partial x_i}(\mathbf{x}, \mathbf{x}_s, \omega)\right)\left(\frac{\partial \tilde{\Psi}_i}{\partial x_j}(\mathbf{x}, \mathbf{x}_s, \omega) + \frac{\partial \tilde{\Psi}_j}{\partial x_i}(\mathbf{x}, \mathbf{x}_s, \omega)\right)\right]. \tag{6}$$

Hereby $\tilde{u}_i$ and $\tilde{\Psi}_i$ are the forward and backpropagated displacements in frequency domain, respectively. The backpropagated wavefield Ψ_i in time domain is defined as

$$\Psi_i(\mathbf{x}, \mathbf{x}_s, t) = \sum_{receivers} \int dt G^{ip}(\mathbf{x}, t, \mathbf{x}_r, \tau) \delta u_p(\mathbf{x}_r, T - \tau) \quad (p = 1, 2, 3). \tag{7}$$

This wavefield is thus generated at the receivers by the residual reversed in time acting as source time function. Hereby G^{ip} is the Green's function for displacement and T denotes the total time length. The transformation of wavefields from time to frequency domain is performed on the fly as done by Sirgue et al. (2008)

$$\tilde{u}_i(\mathbf{x}, \omega) = \sum_{l=0}^{nt} \exp(i\omega l \Delta t) u_i(\mathbf{x}, l\Delta t) \Delta t, \tag{8}$$

where nt is the number of timesteps and Δt the time sampling.
Several advantages arise from the calculation of gradients in the frequency domain. For the inversion only a

few discrete frequencies are generally sufficient for the model reconstruction. Thus, storage costs of wavefields decrease dramatically compared to time domain. At the same time 3D modeling of elastic wavefields is more efficient in the time domain. The time-frequency approach thus enables an optimisation of runtime and storage costs. Furthermore it allows an easy frequency filtering and flexible time windowing during the inversion process.
The modeling is performed with a classical time-domain elastic finite-difference code discretizing the velocity stress formulation of the elastic wave equation on a staggered grid (Virieux, 1986). Boundary reflections are efficiently reduced applying convolutional perfectly matched layers (Kamatitsch and Martin, 2007). The code is optimised for parallel computing architectures (Bohlen, 2002).
We calculate the derivatives of the displacement components u_i in the equations (4) to (6) directly from the particle velocity components v_i, not from stress components as it is often done for velocity-stress formulations (e.g. Shipp and Singh, 2002; Köhn et al., 2012). To derive displacements we can use the simple relation

$$u_i(\mathbf{x}, \omega) = \frac{1}{i\omega} v_i(\mathbf{x}, \omega). \tag{9}$$

This has the advantage, that only three wavefield components instead of nine need to be stored and additionally no medium parameters are required for the gradient computation of $\delta\lambda$, $\delta\mu$ and $\delta\rho$. Spatial derivatives of u_i in the equations (5) and (6) are calculated with the use of finite differences.
It is often favourable to use the P-wave velocity v_p, the S-wave velocity v_s and the density ρ as parametrisation (Köhn et al., 2012). The corresponding gradients can be derived from the equations (4) to (6) by applying the chain rule, leading to

$$\delta v_p = 2\rho v_p \delta\lambda, \tag{10}$$

$$\delta v_s = -4 v_s \rho \delta\lambda + 2 v_s \rho \delta\mu \tag{11}$$

$$\delta\rho' = (v_p^2 - 2v_s^2)\delta\lambda + v_s^2 \delta\mu + \delta\rho \tag{12}$$

$\delta\rho'$ is the density gradient in the new parametrisation.

APPLICATIONS

This section shows the results of our first application of 3D full waveform inversion (FWI) to invert 3D subsurface structures by using two different transmission geometries: an ideal 3D geometry and a more realistic 2D geometry, resembling two boreholes. Results obtained for a checkerboard and a random medium model are shown. Furthermore, a comparison between 3D FWI and 2D FWI was performed for the random medium. Table 1 lists the seven different tests which will be compared here, varying in model, acquisition geometry, number of receiver components and dimensionality of the FWI.

	model	FWI	acquisition geometry	inverted frequencies (Hz)	S-wave-lengths (m)	P-wave-lengths (m)	number of iterations
Test 1	3D checker	3D	3D, 3C	$140 \rightarrow 240$	$25 \rightarrow 15$	$45 \rightarrow 26$	37
Test 2	3D checker	3D	2D, 3C	$160 \rightarrow 240$	$22 \rightarrow 15$	$39 \rightarrow 26$	70
Test 3	3D random	3D	3D, 3C	$140 \rightarrow 320$	$25 \rightarrow 11$	$45 \rightarrow 20$	73
Test 4	3D random	3D	2D, 3C	$100 \rightarrow 320$	$35 \rightarrow 11$	$63 \rightarrow 20$	75
Test 5	3D random	3D	2D, 1C	$100 \rightarrow 320$	$35 \rightarrow 11$	$63 \rightarrow 20$	73
Test 6	2.5D random	2D	2D, 2C	< 320	> 11	> 20	36
Test 7	3D random	2D	2D, 2C	< 320	> 11	> 20	66

Table 1: Inversion tests varying in method, models, acquisition geometry and number of components (C) with applied inversion parameters.

Model and acquisition geometry

The model size is $240\,\mathrm{m} \times 160\,\mathrm{m} \times 280\,\mathrm{m}$, that is $300 \times 200 \times 350$ gridpoints in X-, Y- and Z- direction, respectively. The grid spacing is $dh = 0.8\,m$. Average material parameters of the real models were adapted with $v_p = 6300\,\frac{\mathrm{m}}{\mathrm{s}}$, $v_s = 3500\,\frac{\mathrm{m}}{\mathrm{s}}$ and $\rho = 2800\,\frac{\mathrm{kg}}{\mathrm{m}^3}$. The seismic velocities show checkerboard or

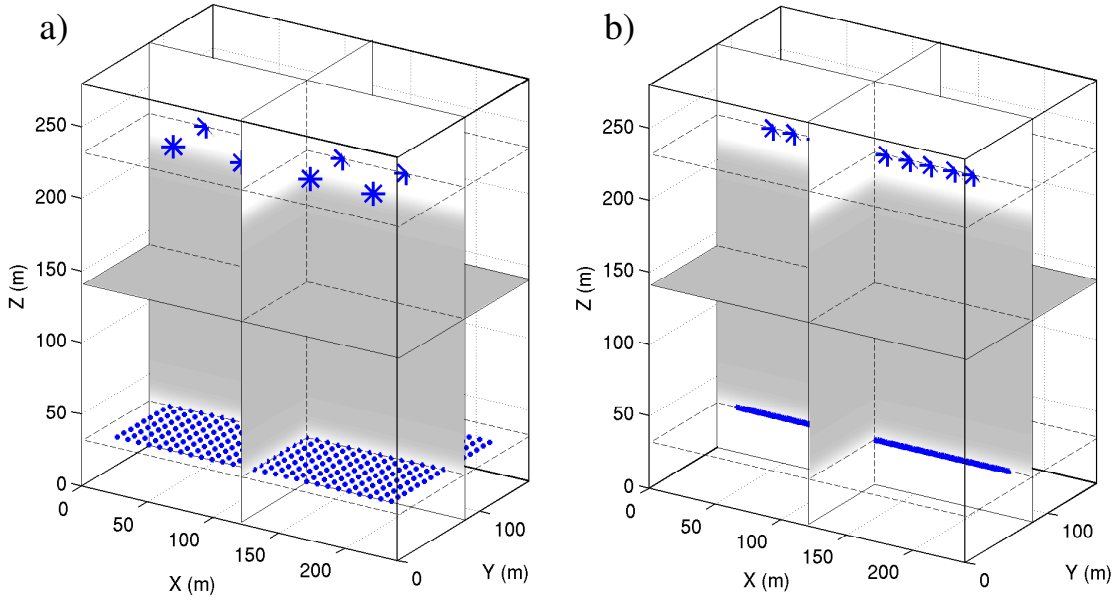

Figure 1: Acquisition geometries. Source and receiver positions are indicated by stars and crosses, respectively. a) 3D geometry with 12 sources and 416 receivers; b) 2D geometry with 10 sources and 100 receivers

random medium structures whereas the density is kept homogeneous and constant during inversion.

The acquisition geometries are shown in Figure 1. The grey area corresponds to checkerboard or random medium structure, which changes to homogeneous medium (white area) towards source and receiver planes. For the 3D acquisition geometry (Figure 1a) 416 receivers and 12 sources, marked as crosses and stars, respectively, were regularly arranged in X-Y oriented source and receiver planes. This configuration is used to test the performance of the 3D FWI in favourable geometry. For the 2D acquisition geometry only a line of 10 sources and a 200 m distant line of 100 receivers at $Y = 80$ m was used, as indicated in Figure 1b. Compared to the 3D geometry, additional sources and receivers were added in these lines to increase the coverage. With this geometry, the reconstruction of 3D structures using a 2D geometry is tested and compared to 2D FWI results. We applied point forces in Z-direction with a central source frequency of 200 Hz, emitting both P- and S-waves. Generally, we used all three receiver components in the 3D inversion and the X- and Z-component in the 2D inversion.

Inversion setup

We inverted for v_p and v_s as given in the equations (10) and (11) and chose homogeneous starting models, hereby adapting the average seismic velocities. The gradients were tapered around source and receiver planes and along the model boundaries to avoid artefacts in these areas. The different tests and the respective inversion parameters, like the number of iterations and the frequency range of the FWI, are listed in Table 1. For the 3D FWI up to three frequencies per iteration were used, which were successively increased in 20 Hz steps. The 2D FWI is performed with an elastic FWI code developed by Köhn (2011). This code is based on the adjoint gradient method similarly to the 3D code, however, it calculates gradients in time domain. It therefore uses the full frequency spectrum. For the 2D calculations a lowpass filter of 320 Hz was applied in all tests.

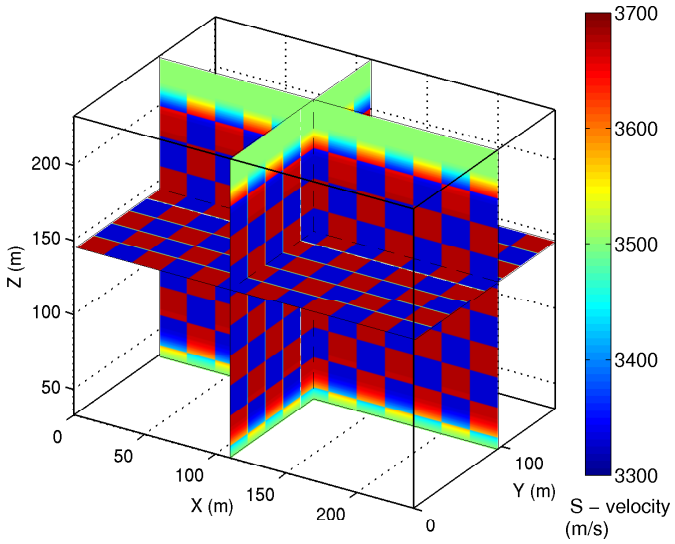

Figure 2: Checkerboard model v_s with 20 m edge length and $\pm 5\%$ velocity perturbations. The source-receiver plane of the 2D acquisition geometry at $Y = 80$ m is indicated by a white dashed line.

The checkerboard test

The checkerboard model (Figure 2) consists of alternating cubes of 20 m edge length and $\pm 5\%$ velocity variation in both v_p and v_s. The checkerboard is chosen antisymmetric to the 2D geometry source-receiver plane at $Y = 80\,m$, indicated with a white dashed line in Figure 2. Note that the Y-Z slice shown here is 12 m distant from this plane.

Inversion parameters used for FWI with 3D geometry (test 1) and 2D geometry (test 2) are given in Table 1. We used a minimum frequency of 140 Hz (S-wavelength 25 m) and increased it in 20 Hz steps to 240 Hz (S-wavelength 15 m), employing three frequencies at a time. This frequency range turned out to be not sufficient to resolve v_p. We will therefore show results for v_s only. The inversion for the 2D acquisition geometry required about twice the number of iterations to converge compared to the 3D geometry.

The models inverted using data acquired with 3D and 2D geometries are plotted in Figure 3. When using data of a 3D source-receiver geometry (Figure 3a), the inversion can resolve the cubes well. The inversion is not able to resolve the sharp edges, as this would require the use of higher frequencies. The 3D FWI of data acquired with a 2D source-receiver geometry is capable to reconstruct the checkerboard pattern in the area adjacent to source-receiver plane (Figure 3b). Structures up to 40 m apart from the plane, which corresponds to about two wavelengths, could be recovered. Furthermore, the antisymmetric pattern of the checkerboard could be resolved. However, resolution is less than for the 3D geometry, which is due to the lower wave path coverage. This example indicates that 3D FWI is capable to recover 3D structures in the vicinity of the direct propagation path and also structures outside the first Fresnel zone of the direct rays.

The random medium test

To derive a realistic model with relatively simple wavefields for our first application we chose a random medium model. We used statistical parameters as observed for crystaline rocks at the German Continental Drilling site (KTB) (Kneib, 1995). The random medium (Figure 4) is described by an exponential autocorrelation function in space with a correlation length of 30 m and a standard deviation of 5% for the Gaussian distributed seismic velocities. The average velocities are the same as in the previous section with $v_p = 6300\,\frac{\mathrm{m}}{\mathrm{s}}$ and $v_s = 3500\,\frac{\mathrm{m}}{\mathrm{s}}$ and a constant v_p/v_s ratio of 1.8. The model features differently sized 3D structures and is used here to test resolution of the FWI results for different scales.

Results 3D full waveform inversion:

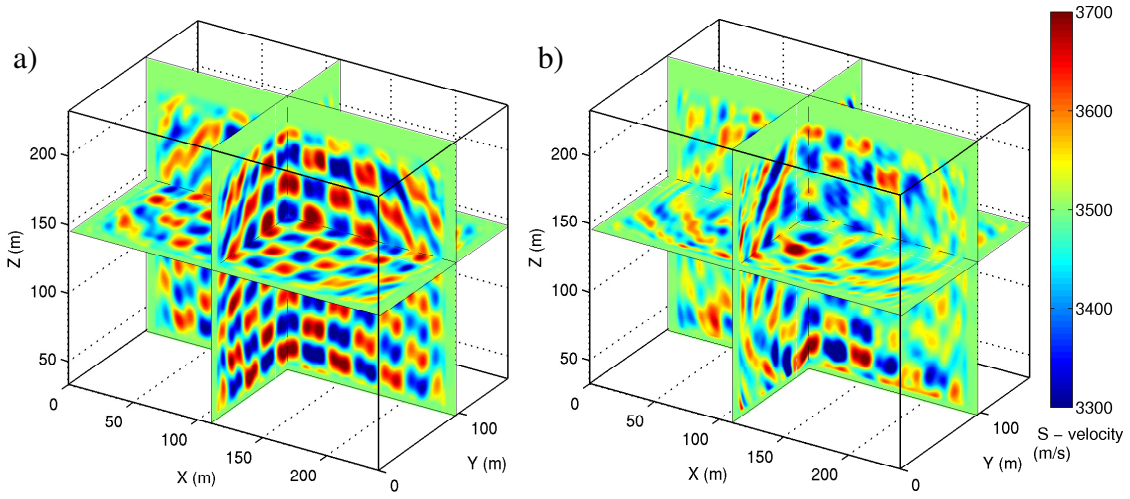

Figure 3: Checkerboard inversion results for data acquired with a) 3D geometry (Figure 1a), test 1 and b) 2D geometry (figure 1b), test 2.

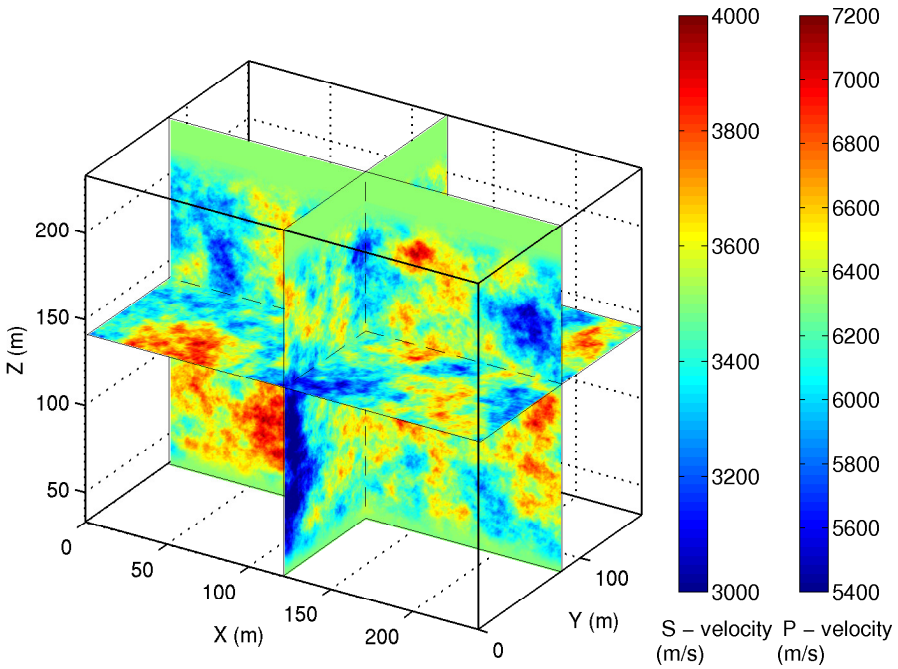

Figure 4: The random medium velocity model.

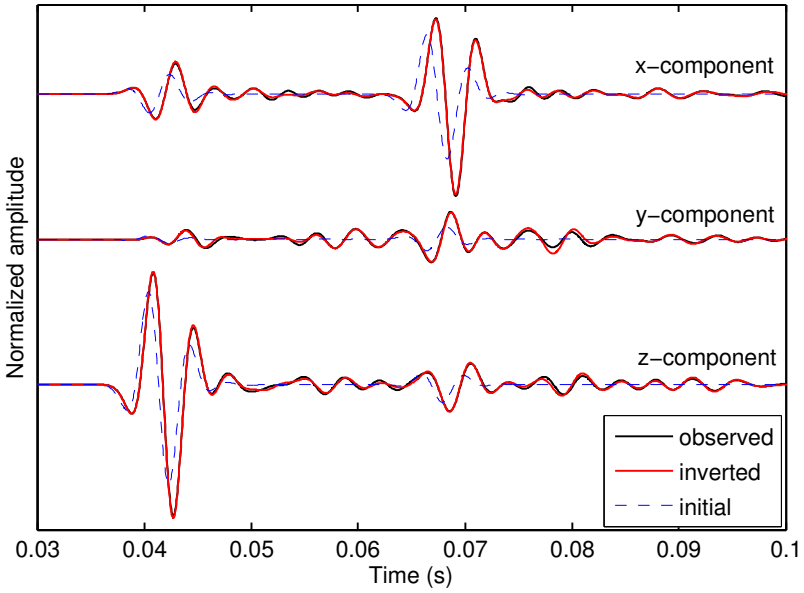

Figure 5: Observed, initial and inverted waveforms of 3D FWI with 3D acquisition geometry data (test 3) at one representative receiver (136 m, 72 m, 32 m) and for one shot at (96 m, 80 m, 232 m).

Inversion parameters are given in Table 1, test 3. The maximum S-wavelength of 25 m corresponds to half the size of the largest model structures. The smallest wavelengths are 20 m and 11 m of P- and S-waves, respectively. For the 2D acquisition geometry (test 4) lower frequencies of down to 100 Hz corresponding to S-wavelengths of about 35 m were required for the inversion to succeed.

The misfit was successfully decreased to final values of 1.5% of the initial misfit for the 3D geometry data and 2.2% for the 2D geometry data. Figure 5 shows the observed, initial and inverted 3-component waveforms at one exemplary receiver and for one shot. Starting from a homogeneous model, the main phases of P- and S-waves as well as the scattered waves in the observed data can be well explained by the final model for all components.

In Figure 6a and Figure 6b the final inverted models of v_s and v_p for the 3D acquisition data are plotted. Compared to the true model in Figure 4, the differently sized 3D structures of the random medium are well resolved in v_s. Structures smaller than the minimum wavelength could be recovered. The v_p model is smoother due to its larger wavelengths. The quality decreases towards the model boundaries where wavefield coverage is lower.

The v_s model obtained for the 2D acquisition geometry data is shown for comparison in Figure 6c. Maximum wave path coverage is along the source-receiver plane at $Y = 80$ m. In this plane the main structures are recovered by the inversion. However, even though we used a denser spacing of sources and receivers within this plane, the quality is less than for the FWI with 3D geometry data. Similar to the checkerboard test, we observe that the 3D FWI succeeds to reconstruct 3D structures outside the source-receiver plane. Using multi-component 3D scattered waves, some structures up to two wavelengths apart from the plane are recovered.

Highest amplitudes of the S-wave in the source-receiver plane are found on the X-component seismograms. We repeated the 3D FWI with 2D source-receiver geometry using only the X-component of the observed data to see the influence of multi-component data (test 5). The final v_s model is plotted in Figure 6d. Within source-receiver plane the reconstructed structures look quite similar to the three component result in Figure 6c. The main difference is, that gradients and model updates of the X-component inversion are symmetric to source-receiver plane. Structures antisymmetric to source-receiver plane cannot be resolved correctly without the additional information about the Y-component waveforms.

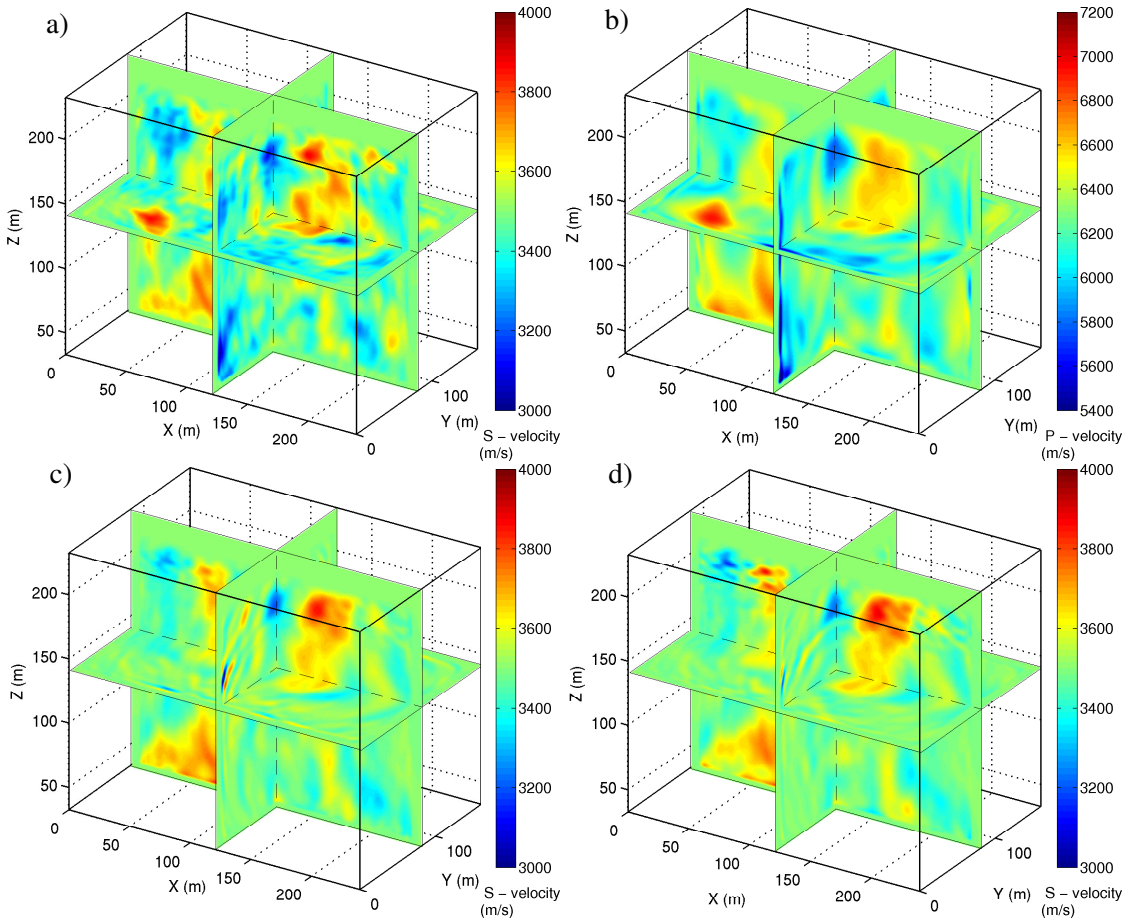

Figure 6: 3D FWI results for the random medium model using different acquisition geometries: a) model v_s inverted with 3D geometry (test 3), b) model v_p inverted with 3D geometry (test 3), c) model v_s inverted with 2D geometry using all receiver components (test 4) and d) model v_s inverted with 2D geometry using one receiver component (x-component)(test 5).

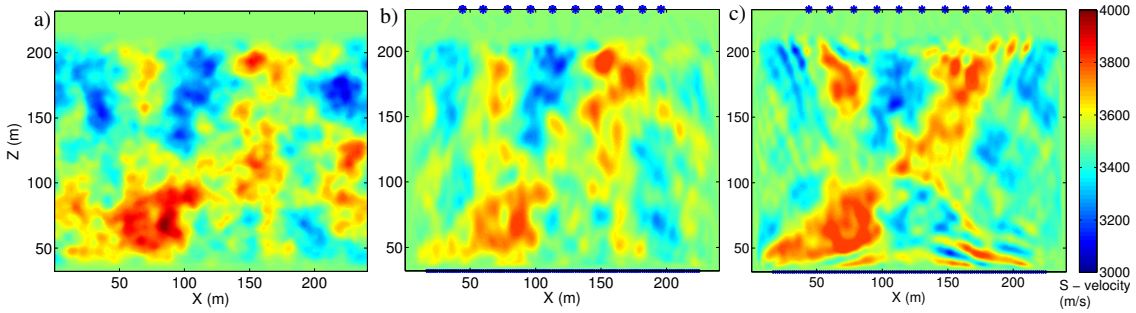

Figure 7: Reconstruction of v_s using 2D FWI; sources (stars) and receivers (crosses) are marked. a) real smoothed model, b) result 2D FWI of 2.5D random medium data (test 6) as reference and c) result 2D FWI of 3D random medium data (test 7)

Comparison of 3D and 2D inversion results:

In many applications 2D FWI is applied to cross-well seismic experiments (e.g. Pratt et al., 2005; Zhang et al., 2012). In these studies structures outside the acquisition plane are neglected but may distort the inversion results. To study the possible site effects of 3D structure we compare the 3D FWI results with the results of a 2D FWI. For the 2D FWI we used the same 2D acquisition geometry as previously. We thus try to resolve the plane at $Y = 80\,\text{m}$ of the random medium. Two tests were performed: test 6 and test 7 (Table 1). As a reference result a 2D FWI of 3D modelled data of the 2.5D random medium was performed (test 6). The 2.5D model extends model parameters at Y=80 m of the random medium constant in Y-direction. The data of this model are thus not influenced by 3D scattering and a 2D approximation is valid. In test 7 the data of the 3D random medium were inverted, which contain the 3D scattered waves.

To invert the 3D data with a 2D method, a transformation of observed data from 3D to 2D was applied to account for the differences between line source and point source wavefields. We convolved seismograms with $\frac{1}{\sqrt{t}}$ as phase correction and multiplied amplitudes with $C\sqrt{t}$ as amplitude correction (Pica et al., 1990). The transformed 3D modelled data for the 2.5D model show a very good agreement with the 2D data modelled for the plane at $Y = 80\,m$. This proves, that the transformation works well for the given scenarios.

We applied a 2D FWI to the transformed data of the 2.5D model and of the 3D model. In both cases the 2D inversion successfully minimized the misfit to 1-2% of the initial value.

The 2D FWI results for v_s are shown in Figure 7. The slice of the true model (Figure 7a) is smoothed, to enable a better comparison. The 2D FWI of the 2.5D model data (Figure 7b) successfully recovered the random medium structure. Its quality and resolution is comparable to the 3D FWI result achieved with 3D source-receiver geometry (Figure 6a). The main features can still be reconstructed when inverting the data of the 3D heterogeneous random medium with 2D FWI (Figure 7c). However, smaller structures suffer in resolution and artefacts are caused by 3D site-scattering. This can be explained when looking at the effects of 3D scattering on the waveforms. Figure 8a shows a comparison between the 2.5D random medium data without 3D scattering versus the 3D random medium data with 3D scattering for X-, Y-, and Z-component at one exemplary receiver. 3D scattering has a significant influence on the wavefields. In Figure 8b the observed, initial and inverted waveforms of the 2D FWI are plotted and it is evident, that the 2D FWI tries to fit the 3D scattered waveforms. However, the 2D FWI is unable to interpret the 3D scattering correctly, leading to artefacts and the lack of resolution. The resolution of 2D FWI thus suffers from the presence of 3D small scale heterogeneities.

A 3D FWI with 2D source-receiver geometry (test 4) has the advantage to gain information about 3D structures outside source-receiver plane, as was shown in the previous section. A comparison of the final model achieved with 3D FWI (Figure 6b) and the 2D FWI result of the 3D random medium (Figure 7c)) shows, that the resolution within source-receiver plane is comparable.

Table 2 gives a comparison of the computation times for 2D FWI and 3D FWI. The 2D FWI requires only about 64 core hours in total for our example and was performed on a 8 CPU workstation. The 3D FWI

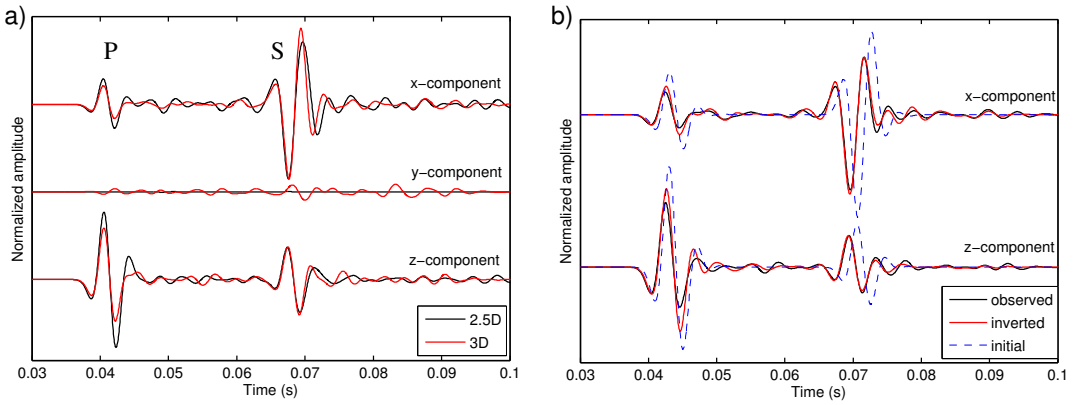

Figure 8: Waveforms at receiver (111 m, 80 m, 32 m) for source location (96 m, 80 m, 232 m): a) The comparison of waveforms for the 3D and the 2.5D random medium model shows the influence of 3D scattering. b) Observed, initial and final inverted waveforms of the 2D FWI with 3D random medium data (test 7).

3D FWI	800 cores	73 iterations	$300 \times 200 \times 350$	35 hours
2D FWI	8 cores	67 iterations	300×350	8 hours

Table 2: Comparison of run times for a 2D and a 3D elastic FWI using 10 sources, 28 forward modelings per iteration and 3300 timesteps.

requires 28.000 core hours and can be realized nowadays on high performance computers.

CONCLUSION

We present an implementation of 3D elastic full waveform inversion (FWI) which is based on the adjoint method and uses a time-frequency approach. First applications confirm the efficiency of this approach, which shows for example in a dramatic reduction of wavefield storage and an efficient calculation of 3D wavefields. We discussed the performance of the code for a random medium and a checkerboard example in transmission configuration. Using a 3D acquisition geometry, the 3D elastic FWI can successfully recover the 3D velocity structures starting from a homogeneous starting model. Using a 2D acquisition geometry 3D structures are recovered up to 1 to 2 wavelengths adjacent to the source-receiver plane, however with less resolution. When using only one component directed parallel to the source-receiver plane, the inversion result is symmetric and structures antisymmetric to this plane cannot be reconstructed correctly. The results indicate, that the application of 3D FWI to multi-component cross-well data might be used to detect 3D structures in an area around the acquisition plane. For comparison a 2D FWI was performed. In the presence of 3D small-scale heterogeneities the 2D FWI suffers in resolution and from artefacts due to 3D scattering effects, still, the main structures in the acquisition plane are resolved.

ACKNOWLEDGMENTS

The work was performed within the project TOAST which is part of the GEOTECHNOLOGIEN program, funded by the German Ministry of Education and Research (BMBF) and the German Research Foundation (DFG), grant 03G0752A
This work was kindly supported by the sponsors of the *Wave Inversion Technology (WIT) Consortium*.
The calculations were performed on the JUROPA cluster at Jülich supercomputing center and on the Cray XE6 at HLRS, Stuttgart.

REFERENCES

Bohlen, T. (2002). Parallel 3-D viscoelastic finite difference seismic modeling. *Computers and Geoscience*, 28:887–889.

Epanomeritakis, I., Akcelik, V., Ghattas, O., and Bielak, J. (2008). A newton-cg method for large-scale three-dimensional elastic full-waveform seimic inversion. *Inverse Problems*, 24:26pp.

Etienne, V., Hu, G., Operto, S., Virieux, J., Barkved, O., and J.H., K. (2012). Three-dimensional acoustic full waveform inversion - algorithm and application to valhall. In *Extended Abstracts, 74th EAGE meeting*, Copenhagen, Denmark. P343.

Fichtner, A., Kennett, B., Igel, H., and Bunge, H.-P. (2009). Full seismic waveform tomography for upper-mantle structure in the australasian region using adjoint methods. *Geophysical Journal International*, 179:1703–1725.

Groos, L., Schäfer, M., Forbriger, T., and Bohlen, T. (2012). On the significance of viscoelasticity in a 2d full waveform inversion of shallow seismic surface waves. In *Extended Abstracts, 74th EAGE meeting*, Copenhagen, Denmark. C011.

Kamatitsch, D. and Martin, R. (2007). An unsplit convolutional perfectly matched layer improved at grazing incidence for the seismic wave equation. *Geophysics*, 72(5):SM155–SM167.

Kneib, G. (1995). The statistical nature of the upper continental crystalline crust derived from in situ seismic measurements. *Geophysical Journal International*, 122:594–616.

Köhn, D. (2011). Time domain 2d elastic full waveform tomography. dissertation, Christian-Albrechts-Universität zu Kiel.

Köhn, D., De Nil, D., Kurzmann, A., Przebindowska, A., and Bohlen, T. (2012). On the influence of model parametrization in elastic full waveform tomography. *Geophysical Journal International*, 191:325–345.

Mora, M. (1987). Nonlinear two-dimensional elastic inversion of multioffset data. *Geophysics*, 52(9):1211–1228.

Pica, A., Diet, J., and Tarantola, A. (1990). Nonlinear inversion of seismic reïňĆection data in a laterally invariant medium. *Geophysics*, 55(3):284–292.

Plessix, R.-E. (2009). Three-dimensional frequency-domain full-waveform inversion with an iterative solver. *Geophysics*, 74(6):WCC149–WCC157.

Pratt, R., Chin, C., and Hicks, G. (1998). Gauss-newton and full newton methods in frequency-space seismic wavefrom inversion. *Geophysical Journal International*, 133:341–362.

Pratt, R., Hou, F., Bauer, K., and Weber, M. (2005). Cross-well seismic waveform tomography for monitoring co_2 injection: a case study fom the ketzin site, germany. *in Scientific Results from the Mallik 2002 Gas Hydrate Production Research Well Program, Mackenzie Delta, Northwest Territories, Canada*, 585:14p.

Pyun, S., Shin, C., Lee, H., and Yang, D. (2008). 3d elastic full waveform inversion in the laplace domain. In *Extended Abstract, SEG Annual Meeting*, Las Vegas, Nevada. 2008-1976.

Sheen, D.-H., Tuncay, K., Baag, C.-E., and Ortoleva, P. (2006). Time domain gauss-newton seismic waveform inversion in elastic media. *Geophysical Journal International*, 167:1373–1384.

Shipp, R. and Singh, S. (2002). Two-dimensional full waveïňĄeld inversion of wide aperture marine seismic streamer data. *Geophysical Journal International*, 151:325–344.

Sirgue, L., Barkved, O., Dellinger, J., Etgen, J.and Albertin, U., and Kommedal, J. (2010). Full waveform inversion: the next leap forward in imaging at valhall. *First Break*, 28:65–70.

Sirgue, L., Etgen, J., and Albertin, U. (2008). 3d frequency domain waveform inversion using time domain finite difference methods. In *Extended Abstracts, 70th EAGE meeting*, Rome, Italy. F022.

Tape, C., Liu, Q., Maggi, A., and Tromp, J. (2010). Seismic tomography of the southern california crust based on spectral-element and adjoint methods. *Geophysical Journal International*, 180:433–462.

Tarantola, A. (1984). Linearized inversion of seismic reflection data. *Geophysical Prospecting*, 32:998–1015.

Tarantola, A. (1988). Theoretical background for the inversion of seismic waveforms, including elasticity and attenuation. *Pure and Applied Geophysics*, 128(1/2):365–399.

Vigh, D., Kapoor, J., Moldoveanu, N., and Li, H. (2011). Breakthrough acquisition and technologies for subsalt imaging. *Geophysics*, 76(5):WB41–WB51.

Virieux, J. (1986). P-sv wave propagation in heterogeneous media: velocity-stress finite difference method. *Geophysics*, 51(4):889–901.

Virieux, J. and Operto, S. (2009). An overview of full-waveform inversion in exploration geophysics. *Geophysics*, 74(6):WCC1–WCC26.

Zhang, F., Juhlin, C., Cosma, C. amd Tryggvason, A., and Pratt, R. (2012). Cross-well seismic waveform tomography for monitoring co_2 injection: a case study fom the ketzin site, germany. *Geophysical Journal International*, 189:629–646.